Broadband, site selective and time resolved photoluminescence spectroscopic studies of finely size-modulated $Y_2O_3:Eu^{3+}$ phosphors synthesized by a complex based precursor solution method

Sudeshna. Ray [a,b*], Sergio Fabián León-Luis [c], Francisco Javier Manjón [a,] , Miguel Alfonso Mollar [a], Oscar Gomis [d], Ulises Ruyman Rodríguez-Mendoza [c], Said Agouram [e], Alfonso Muñoz [f], Victor Lavin [c]

[a] Instituto de Diseño para la Fabricación y Producción Automatizada and MALTA Consolider Team, Universitat Politècnica de València, 46022 València, Spain.

[b] Department of Applied Chemistry, National Chiao Tung University, Hsinchu 300, Taiwan.

[c] Departamento de Física Fundamental y Experimental, Electrónica y Sistemas and MALTA Consolider Team, Universidad de La Laguna, 38200 San Cristóbal de La Laguna, Santa Cruz de Tenerife, Spain.

[d] Centro de Tecnologías Físicas and MALTA Consolider Team, Universitat Politècnica de València, 46022 València, Spain.

[e] Departamento de Física Aplicada y Electromagnetismo, Universitat de València, 46100 Burjassot, València, Spain.

[f] Departamento de Física Fundamental II, Instituto de Materiales y Nanotecnología and MALTA Consolider Team, Universidad de La Laguna, 38200 San Cristóbal de La Laguna, Santa Cruz de Tenerife, Spain.

ABSTRACT

Undoped and Eu^{3+}-doped cubic yttria (Y_2O_3) nanophosphors of good crystallinity, with selective particle sizes ranging between 6 to 37 nm and showing narrow size distributions, have been synthesized by a complex-based precursor solution method. The systematic size tuning has been evidenced by transmission electron microscopy, X-ray diffraction, and Raman scattering measurements. Furthermore, size-modulated properties of Eu^{3+} ions have been correlated with the local structure of Eu^{3+} ion in different sized $Y_2O_3:Eu^{3+}$ nanophosphors by means of steady-state and time-resolved site-selective laser spectroscopies. Time-resolved site-selective excitation measurements performed in the $^7F_0 \rightarrow {}^5D_0$ peaks of the Eu^{3+} ions at C_2 sites have allowed us to conclude that Eu^{3+} ions close to the nanocrystal surface experience a larger crystal field than those in the nanocrystal core. Under the site selective excitation in the $^7F_0 \rightarrow {}^5D_0$ peaks, energy transfer between the sites has also been observed.

Keywords: nanophosphor; size-modulated synthesis; structure; Raman; photoluminescence; Eu^{3+}

* Corresponding author: Dr. Sudeshna Ray

E mail - sudeshna@cc.nctu.edu.tw , Telephone (work) - +886-3-5731695, Fax - +886-3-57-23764

1. Introduction

Luminescence nanomaterials have gathered enormous technological importance in the new millennium because they may have a number of potential advantages over conventional micron-sized ones. In particular, the image resolution on a cathode ray tube display is closely related to the particle size of the phosphors and it has been established that smaller particles are favorable for higher resolution [1]. Besides, nanophosphors offer the possibility of smoother films with higher packing densities than microphosphors and a larger percentage of cathodoluminescent active materials at low-excitation voltages due to the reduced electron penetration depth [2]. On the other hand, the unique electronic structure and the numerous well defined optical transitions involving the electrons of the 4*f* shell in trivalent rare earth (RE^{3+}) ions embedded in inorganic hosts make them potential candidates for many applications, including lamp phosphors, fiber amplifiers, high density optical storage materials, and electroluminescent display devices [3-7]. Consequently, extensive research efforts have been undertaken on RE^{3+}-doped nanophosphors during the last two decades due to their novel size-dependent optical properties for their potential applications in the photonic and biophotonic fields of research [8].

Yttria (Y_2O_3), with cubic bixbyite structure at ambient conditions, is a transparent material from the UV (230 nm) well into the infrared (~ 8 μm), is optically isotropic and hard, and accepts RE^{3+} ions in the trivalent state without charge compensating problems or ion-size limitations. Besides, Y_2O_3 has one of the smallest frequencies of the dominant phonon (380 cm^{-1}) among the known oxides [9], favoring high quantum efficiencies of the RE^{3+} emitting levels. Therefore, the optical properties of bulk RE^{3+}-doped Y_2O_3 have been extensively studied and have shown that it is an excellent laser host material, with high brightness as a red color phosphor, acceptable atmospheric stability, reduced degradation under applied voltage and lack of hazardous constituents as opposed to sulfide phosphors [10-12] It has a lumen equivalent brightness of 70% relative to 611 nm light and radiant efficiency of approximately

8.7% with better saturation without any detrimental effects [13] and laser action has been observed at 611.3 nm [14]. Owing to the fascinating perspectives of the industrial application of nanophosphors and RE^{3+}-doped yttria, a considerable effort has been made in the last years in the synthesis of $Y_2O_3:Eu^{3+}$ nanoparticles to control and improve the luminescence properties of these nanophosphors [1, 15-22]. It is well known that the optical properties of the RE^{3+} ions are governed by Judd-Offelt (J-O) *f-f* transitions, which depend on the environment of these ions in a host matrix, and due to the static electric field produced by the surrounding charge distribution corresponding to the anion neighbors. The inter-electronic interaction between the electrons of the inner 4*f* shell of the RE^{3+} ions and the charge of the host ligands, all distributed in a particular local point symmetry, is known as the crystal-field (CF) interaction and it rules the fine structure splitting of the free-ion multiplets and the forced intra-configurational 4*f*-4*f* electric-dipole transitions probabilities [23]. Consequently, the luminescence dynamics of the RE^{3+} ions incorporated in nanoparticles, including the spontaneous emission and the energy transfer probabilities, depends on the environment; i.e., the host lattice, the nanoparticle size and shape, the RE^{3+} ion concentration, the symmetry and site occupied by RE^{3+} ions [24-30].

In order to analyze the influence of the RE^{3+} environment on the optical properties of RE^{3+}-doped hosts, the Eu^{3+} ion has usually been used as a structural probe, mainly because of the large sensitivity of its luminescence on the local environment, which takes place mainly in the visible range between the multiplets of the low energy terms, $^5D_0$ and ^7F_J (J=1 4) [31, 32]. However, the most important and unique feature of Eu^{3+} ions is the existence of allowed $^7F_0 \leftrightarrow {}^5D_0$ crystal-field transitions, i.e. transitions between singlet (non-degenerate) levels. [31, 32]. Consequently, it is possible to selectively excite the Eu^{3+} ions in a particular environment in which absorption energy is resonant with a laser light, provided that the laser spectral line-width is much narrower than the inhomogeneous broadening. This technique, known as fluorescence line narrowing (FLN), allows obtaining valuable information about the energy level structure, crystal-field parameters, lifetimes, homogeneous linewidths or energy transfer processes between ions in different environments in the solid [31-35].

In the present work, we report the synthesis of undoped Y_2O_3 and Eu^{3+}- doped Y_2O_3 nanoparticles with selective sizes ranging from 6 to 37 nm, by a complex-based precursor solution method. Crystalline structure, morphology, and vibrational properties of the as-synthesized nanopowders have been studied by means of x-ray diffraction (XRD), transmission electron microscopy (TEM), high-resolution transmission electron microscopy (HRTEM), selective area electron diffraction (SAED), and Raman scattering measurements. Structural characterization witnesses the generation of high quality of the nanophosphors. With the help of lattice dynamics *ab initio* calculations we have analyzed Raman scattering measurements in both doped and undoped nanocrystals and have found evidence of electronic Raman scattering of Eu^{3+} ions in cubic Y_2O_3 nanophosphors, which may substitute Y^{3+} ions in either of two sites C_2 or S_6 (also noted C_{3i}). The photoluminescence properties of Y_2O_3:Eu^{3+} nanoparticles have also been characterized and the fine size-tuning of the Eu^{3+} such properties in nanocrystals is discussed with the help of broadband and time-resolved site-selective optical spectroscopies. In this context, the most interesting point, and one of the novel outcomes of this research, is that the luminescence measurements suggest a continuous variation of the crystal field on Eu^{3+} ions at the C_2 sites in the cubic nanocrystals. Therefore, we propose the existence of different kinds of sites in Y_2O_3 nanocrystals, whose proportion depends on the nanophosphor size: i) undistorted C_2 and S_6 sites, similar to those of bulk Y_2O_3, in the core of the nanocrystals; and ii) continuously-distorted C_2 and S_6 sites at the vicinity of the nanocrystal surface. Moreover, we report the presence of a band at 582.4 nm in all the nanophosphors related to the occupancy of Eu^{3+} in a third site completely different to the 'true' C_2 or S_6 sites, which cannot be associated to other symmetries found in other Y_2O_3 nanophosphors.

In summary, although the synthesis of Y_2O_3 nanoparticles with sizes below 10 nm is not novel, herein, we report a methodology for the fine size-tuning of well-crystallized cubic nanophosphors substantiated by XRD, Raman and Photoluminescence spectroscopies and, to the best of our knowledge, this is the first report of site selective broadband excitation on 6-nm-sized high-quality cubic $Y_2O_3:Eu^{3+}$ nanocrystals, evidencing the occupancy of Eu^{3+} in different sites in small nanophosphors.

2. Experimental Procedure

2.1. Synthesis

Undoped and Eu^{3+}-doped (1 at. wt%) Y_2O_3 nanoparticles were prepared by a complex-based precursor solution method, in which triethanolamine (TEA) was used as a complexing agent [18, 36]. In the synthesis, an aqueous $Y(NO_3)_3$ solution, along with stoichiometric amount of an aqueous $Eu(NO_3)_3$ solution for doped samples, was mixed with the requisite amount of TEA by maintaining metal ion to TEA mole ratio at 1:4. At the beginning, TEA formed a precipitate with metal ions likely due to the formation of metal hydroxides, like yttrium hidroxide [$Y(OH)_3$]. To get a clear solution, this precipitate was dissolved by adding concentrated HNO_3 to the solution. For this purpose the pH must be kept between 3 and 4 because for smaller pH, $Y(OH)_3$ decomposes and a homogenous solution is formed where TEA can make metal-coordinate complexes. The clear solution of TEA-complexed metal nitrate was evaporated on a hot plate by continuous heating at 180–200 ºC with constant stirring that led to foaming and puffing. During evaporation, the nitrate ions provide an *in situ* oxidizing environment for TEA, which partially converts the hydroxyl groups of TEA into carboxylic acids. Upon complete dehydration, the nitrates themselves decomposed with the evolution of brown fumes of nitrogen dioxide, leaving behind a voluminous, organic-based, black, fluffy powder, i.e., the precursor powder. Complete evaporation of the precursor solution resulted in a highly branched polymeric structure, with the metal ions homogeneously lodged in its matrix and thus preventing the segregation of nanoparticles. homogeneously lodged in its matrix and thus preventing the segregation of nanoparticles.

The precursor mass was then divided into four parts and subsequently calcined and annealed at different temperatures like 500 ºC, 600 ºC, 800 ºC and 1000 ºC for 2 h in order to obtain the undoped and Eu^{3+} doped Y_2O_3 nanoparticles of different sizes.

2.2. Morphological, structural, vibrational and optical characterization

Morphology, size, size dispersion, and structure of the nanocrystals at ambient conditions were analyzed by high-resolution transmission electron microscopy (HRTEM), and selected area electron diffraction (SAED) with a Tecnai G2 F20 field emission gun TEM under an acceleration voltage of 200 kV. Samples for HRTEM measurements were deposited onto 300 mesh copper TEM grids coated with 50 nm carbon films. Nanocrystals dispersed in acetone were placed on the grid dropwise. The excess liquid was allowed to evaporate in air.

Structural characterization and phase identification of the nanopowders was carried out by powder XRD measurements with a Rigaku Ultima IV diffractometer equipped with a vertical goniometer and the Cu *Kα* (1.5406 Å) as the incident radiation source.

Vibrational properties of the Y_2O_3 nanophosphors were studied by means of Raman scattering measurements performed with a HORIBA-Jobin Yvon LabRam HR UV microspectrometer with a thermoelectrically-cooled CCD camera using the 632.81 nm line of an He-Ne laser with a resolution better than 2 cm^{-1}.

Luminescence properties of Eu^{3+}-doped Y_2O_3 nanopowders in the visible range were measured after a broadband excitation at 395 nm with a 450 W Xe arc lamp. Emissions were focused with a convergent lens onto a 0.75 m single-grating monochromator (Jobin Yvon Spex 750M) with a resolution of 0.1 nm coupled to a photomultiplier tube (Hamamatsu R928). Time-resolved site-selective excitation and emission spectra were measured by exciting Eu^{3+} ions with a 10 ns pulsed optical parametric oscillator OPO (EKSPLA/NT342/3/UVE) using a digital storage oscilloscope (LeCroy WS424) coupled to the detection system.

2.3. Calculation Details

First principles lattice dynamics calculations were developed to help in the interpretation of Raman scattering measurements in yttria nanoparticles. It is well known that the phase stability and the electronic and dynamical properties of semiconductors are well described by DFT-based total-energy calculations [37]. Therefore, we performed *ab initio* total-energy calculations in bulk Y_2O_3 with the Vienna *ab initio* simulation package (VASP) [38] using the plane-wave method and the pseudopotential theory within the density functional theory (DFT) [39]. The projector-augmented wave scheme (PAW) [40] was implemented in this package to take into account the full nodal character of the all-electron charge density in the core region. Basis set including plane waves up to an energy cutoff of 520 eV were used in order to achieve accurate, highly converged results and an accurate description of the electronic properties. The description of the exchange-correlation energy was performed with the generalized gradient approximation (GGA) with the PBEsol [41] prescription. A dense special k-point sampling for the Brillouin Zone (BZ) integration was performed in order to obtain very well converged energies and forces. The structure was fully relaxed to their equilibrium configuration through the calculation of the forces and the stress tensor. In the relaxed equilibrium configuration, the forces on the atoms are less than 0.004

eV/Å and the deviation of the stress tensor from a diagonal hydrostatic form is less than 0.1 GPa.

Lattice dynamics calculations of phonon modes were performed at the zone centre (Γ point) of the Brillouin zone. For the calculation of the dynamical matrix at the Γ point we used the direct method [42] that involves a separate calculation of the forces in which a fixed displacement from the equilibrium configuration of the atoms within the primitive unit cell is considered.

3. Results and Discussion

3.1. Structural and morphological properties

As already commented, bulk Y_2O_3 usually crystallizes in the cubic bixbyite phase (space group T_h^7, Ia-3), which is one of the typical structures of RE^{3+} sesquioxides (C-type). In this structure, Y ions are surrounded by six O ions generating an assembly of two types of distorted YO_6 octahedra since there are two possible positions for the Y ion: i) a site with inversion symmetry of S_6 (or C_{3i}) local point symmetry and, ii) a site with no inversion symmetry of C_2 local point symmetry, both highlighted in Fig. 1. Since there are 24 C_2 (24d) sites and 8 S_6 (8b) sites in the unit cell, there are three times more Y^{3+} ions at C_2 sites than at S_6 sites, whereas O atoms are located at 48e sites with C_1 point symmetry. On the other side, a metastable monoclinic structure can be obtained after quenching from high pressures and temperatures in micron-sized Y_2O_3 particles [43], despite the stable structure at ambient conditions is the cubic bixbyite structure.

The morphology and sizes of Eu^{3+}-doped and undoped yttria nanoparticles have been analyzed by means of HRTEM measurements. All nanoparticles have mainly spherical shape as shown in Fig. 2(a). The average sizes of samples annealed at 500, 600, 800, and 1000 ^{o}C for 2 h have been estimated by measuring over 100 particles to be 6, 13, 21, and 37 nm, respectively. It is worth noting that the size dispersion obtained from the full width at half maximum (FWHM) of the size distribution peak of each batch is found to be less than ±15% of the average size [as shown in Fig. 2(b)]. Thus quite sharp and narrow distributions of nanoparticles are synthesized by the proposed method. From the HRTEM image shown in Fig. 2(c) the lattice spacing between different layers of doped yttria nanoparticles of 6 nm was calculated to be 3.2 Å, which likely corresponds to the (222) plane of cubic phase Y_2O_3. The distance between the planes corresponding to (222) plane in bulk Y_2O_3 is 3.05 Å, which is smaller than the distance obtained for the nanocrystal annealed at 500 ºC. Thus, from HRTEM pictures of undoped and doped yttria nanoparticles, we can conclude that for both cases the distance between lattice planes is larger for the nanoparticles, indicating an increase in the lattice parameter of the nanoparticles accompanied by the decrease in their sizes. HRTEM pictures indicate the good quality of the 6 nm sized $Y_2O_3:Eu^{3+}$ samples annealed at the rather low temperature of 500 ºC. This is further confirmed by the rather narrow rings obtained by SAED (Fig. 2(d)).

Fig. 3 shows the XRD patterns of Eu^{3+}-doped yttria nanoparticles obtained after different annealing temperatures. They exhibit only peaks consistent with cubic phase (JCPDS 43-1036) and no additional peaks of other phases, like monoclinic Y_2O_3 and Eu_2O_3 [44], or broadband contributions from an amorphous phase have been observed even in the smallest nanoparticles synthesized. Similar XRD patterns are obtained for undoped yttria nanoparticles (not shown). It is worth noting that the XRD patterns of Eu^{3+}-doped and undoped yttria nanophosphors annealed at 1000 ºC are similar to those reported in the literature for bulk single crystal yttria.

Two major effects were noted in the XRD patterns of both undoped and Eu^{3+}-doped yttria as the size of the nanophosphors decreases: i) a shift of XRD peaks towards smaller angles, and ii) a drastic increase in their FWHMs (presented in left inset of Fig. 3). While this second effect is consequence of the decrease of the nanocrystal size, the first effect can be explained by an increase in the lattice parameter as the nanoparticle size decreases. The right inset of Fig. 3 shows the change of the lattice parameter obtained for $Y_2O_3:Eu^{3+}$ nanoparticles as a function of the nanocrystal size. The lattice parameter of the $Y_2O_3:Eu^{3+}$ nanophosphors increase monotonically from 10.607 Å, which is similar to bulk yttria (a=10.603 Å) [45], for an annealing temperature of 1000 ºC to 10.635 Å for an annealing temperature of 500 ºC. This change in the lattice parameter correlates with the decrease in the size of the particle from 37 nm down to 6 nm on going from 1000 ºC to 500 ºC in the thermal treatment. Thus, the lattice parameter of the $Y_2O_3:Eu^{3+}$ nanoparticles with a diameter of 6 nm is 0.33% larger than that of bulk Y_2O_3. Similarly, the lattice parameter of the undoped Y_2O_3 nanoparticles with a diameter of 6 nm is 0.26% larger than that of bulk Y_2O_3. This increase of the lattice parameter with the decrease in nanocrystal size is in agreement with previous results of $Y_2O_3:Eu^{3+}$ nanoparticles synthesized by other methods [1, 36, 46]. However, unlike other works, it is worth noting that our XRD patterns indicate a very good crystalline quality of all the as-synthesized nanopowders since the main peaks of the cubic phase of yttria can be observed even in the samples with the smallest size (6 nm) despite the increasing broadening of the diffraction peaks. The analysis of the peak broadening with the Hall method has allowed us to estimate that the size of crystallites agrees with that obtained from HRTEM measurements. Furthermore, we have found that the smallest nanocrystals, with sizes below 10 nm, have a strain of ca. 0.2%, whereas strain is negligible for nanocrystals with sizes above 10 nm.

3.2. Vibrational properties

According to group theory [47], the irreducible representation of the optical Raman active modes in cubic Y_2O_3 is: $\Gamma_{op} = 4A_g + 4E_g + 14T_g$. Thus, there are twenty-two Raman-active modes, where E_g and T_g (or F_g) modes are doubly and triply degenerated, respectively.

The Raman-active modes of cubic Y_2O_3 can be divided into fifteen modes ($3A_g$+$3E_g$+$9T_g$) coming the vibration of O ions in the 48e Wyckoff positions and seven modes (A_g+E_g+$5T_g$) coming from the vibration of Y ions in the 24d Wyckoff positions. Curiously, Y ions located at 8b (S_6) sites do not contribute with any Raman-active mode and, therefore, conventional Raman scattering cannot provide information on the occupancy of these sites.

Fig. 4 shows the room temperature Raman spectra of Y_2O_3 (a) and Y_2O_3:Eu^{3+} (b) nanoparticles obtained by annealing at different temperatures. Raman spectra of Y_2O_3 nanocrystals are dominated by the 376 cm^{-1} mode with A_g + T_g symmetry. All the observed Raman modes at around 318, 329, 376, 429, 469, 564 and 591 cm^{-1}, summing a total of 7 Raman-active modes, are consistent with those already reported in the literature for the cubic phase [19]. Therefore, our Raman scattering measurements confirm that all undoped Y_2O_3 nanoparticles crystallize in the cubic bixbyite structure irrespective of the nanocrystal size and that there is no trace of Raman modes of other phases even in the smallest nanoparticles. On the other hand, Raman spectra of Y_2O_3:Eu^{3+} nanoparticles show some extra modes along with the Raman-active modes of the cubic phase. In particular, the intensity of the 429 cm^{-1} mode seems to be greatly enhanced and some peaks at around 452, 491, and 604 cm^{-1} appear in the Raman spectrum of Y_2O_3:Eu^{3+} nanocrystals. These features have been previously reported in Y_2O_3:Eu^{3+} nanoparticles [36] and were attributed to the Eu^{3+} doping effect without further explanation. These results suggest that the lattice vibrations of Y_2O_3 are very sensitive to the presence of Eu^{3+} ions in the sites of the Y^{3+} ions, although XRD patterns could not find differences in the crystal structure between Y_2O_3 and Y_2O_3:Eu^{3+} nanoparticles.

Interestingly, two major effects were noticed in the Raman spectra of both undoped and Eu^{3+}-doped yttria as the size of the nanophosphors decreases: i) a shift of Raman peaks towards smaller frequencies, and ii) an increase in their FWHMs; in particular, many Raman bands become specially more asymmetric at the low-frequency side. These effects can be observed in the inset of Fig. 4(a) and right inset of Fig. 4(b) for the main Raman peak of Y_2O_3 near 329 cm^{-1}. The change in linewidth of the Raman modes can be explained by the inhomogeneous strain broadening associated with the small dispersion in particle size and by phonon confinement [48, 49]. On the other hand, Husson *et al.* has reported an increase of many Raman-active mode frequencies in cubic Y_2O_3 as a result of application of pressure [50]. Since this effect can be ascribed to the contraction of Y-O bonds with increasing pressure, the decrease in the Raman frequencies we have measured at ambient conditions with the decrease in the nanocrystal size is contrary to the effect of pressure and can be ascribed to the elongation of Y-O bonds [45, 50]. In fact, a similar low-frequency shift of the main Raman peaks of sesquioxides has been found on increasing lattice constant [51]. Therefore, this result is indicative of the increase of the lattice parameter of the cubic unit cell with decreasing nanoparticle size and confirms the result observed by XRD as well as HRTEM measurements previously commented.

In order to explore the nature of the extra modes appearing in the Raman spectra of Eu^{3+}-doped Y_2O_3 nanoparticles we have compared the frequencies of the Raman-active modes measured in Y_2O_3 nanocrystals with 37 nm size (those with the lattice parameter most similar to bulk material) with the *ab initio* calculated frequencies for bulk Y_2O_3 at ambient conditions. Our experimental and theoretical frequencies and those of other experimental data reported in the literature are compared in Table I. It is clear that the new bands observed in Eu^{3+}-doped Y_2O_3 nanoparticles do not correspond to any of the first-order Raman-active modes of cubic Y_2O_3. Furthermore, they seem not to correspond to any of the first-order Raman-active modes of monoclinic Y_2O_3 or of Eu_2O_3 clusters [52-54]; otherwise, peaks at other frequencies would be observed**.** Moreover, they cannot be attributed to photoluminescence from Eu^{3+} ions since our laser line (632.8 nm or 15798 cm^{-1}) cannot excite the Eu^{3+} ions from the $^7F_0$ ground state to above the $^5D_0$ level at 17215 cm^{-1}, as will be discussed in the next section. Our *ab initio* calculations, which provide the frequencies of the 16 T_u infrared active modes and the A_u and E_u silent modes, seem to indicate that they do not correspond neither to infrared-active modes nor to silent modes allowed by the loss of the translational symmetry in nanocrystals. Finally, it is rather curious that these extra modes are not observed in Raman spectra of Y_2O_3 nanoparticles doped with either Sm^{3+}, Dy^{3+}, Yb^{3+}, or Er^{3+} [55-57]. Therefore, we are led to think that they are due to the activation of new vibrational modes related to Eu^{3+} ions. They can be related to a resonance effect occurring only for Eu^{3+} ions excited with the red laser, since such an effect seems not to be present even in Y_2O_3:Eu^{3+} nanoparticles excited with blue or green light [58, 59].

In this respect, many papers have reported the occurrence of electronic Raman scattering of rare earths in different hosts when excited with the HeNe laser. In most cases, the frequencies of the modes measured in electronic Raman scattering match with the frequencies of the closest levels of the RE^{3+} ion to the ground state obtained by luminescence measurements, as occurs for the electronic Raman scattering of Eu^{3+} ions in YGG, YVO_4, and Y_2O_3 [60-62]. In other cases, electronic Raman scattering can provide information on RE^{3+} ions at sites showing no luminescence. This is the case of Ce^{3+} ions in Y_2O_3 which shows resonant effects that allow obtaining the energy levels of Ce^{3+} ions located in C_2 or C_3i (S_6) sites depending on the excitation laser energy [63]. Since our Raman measurements do not show the characteristic peaks of the $^7F_1$ levels of the Eu^{3+} ion in C_2 sites in Y_2O_3 [63] the new modes observed in Eu^{3+}-doped samples could be due to levels of the Eu^{3+} ion occupying S_6 sites in Y_2O_3. In particular, the strong mode at 429 cm^{-1} in Y_2O_3:Eu^{3+} nanocrystals can be ascribed to electronic Raman scattering due to the transition between the $^7F_0$ ground state and the highest Stark level of the $^7F_1$ multiplet of the Eu^{3+} ions located in C_{3i} (S_6) sites [64, 65]. Furthermore, the 429 cm^{-1} mode shows a frequency shift and broadening as nanocrystal size decreases similar to that of the main Raman peak of Y_2O_3 as presented in the left inset of Fig.

4(b). Unfortunately, we have not been able to obtain more information regarding the nature of the extra peaks located at 452, 491 and 604 cm^{-1} whose changes of frequency, intensity, and width are more difficult to analyze for the different nanocrystal sizes. Further work is needed to clarify the nature of these bands.

In summary, the presence of Eu^{3+} ions in S_6 sites is confirmed by our Raman spectroscopy measurements. The successive frequency shift as well as increase in the FWHM of the Raman bands of both doped and undoped samples, substantiates the fine size tuning of the nanophosphor as evidenced by XRD. Moreover, using structural arguments for the isomorphic substitution of the Y^{3+} ions by Eu^{3+} ions, it is expected that Eu^{3+} ions in the Y_2O_3 host occupy the C_2 and the S_6 types of sites with approximately equal probability. Consequently, since there are about three times more C_2 sites than S_6 sites it is expected that there are 3 times more Eu^{3+} ions at C_2 sites than at S_6 sites, as already commented.

3.3. Photouminescence properties

Optical spectroscopy, and especially the time-resolved site-selective fluorescence line narrowing (FLN) technique, also allows studying the distribution and the structure of the environments of RE^{3+} ions in solids [31, 32]. For that purpose, it must be taken into account that the optical transitions between any two states of the optically active ion are governed by different selection rules for these two sites. The CF interaction can be expanded in odd and even terms allowed by group theory applied to a particular local symmetry site. The odd CF Hamiltonian is responsible for the mixing of the wavefunctions of the $4f^N$ ground configuration with those of opposite-parity excited configurations and it gives rise to forced electric-dipole optical transitions within the ground configuration, forbidden for the free-RE^{3+} ion. On the other side, the even parity CF Hamiltonian breaks the free-RE^{3+} ion multiplets and gives rise to the hyperfine crystal-field, or Stark, levels structure of the RE^{3+} ion [66]

Consequently, the CF acting on the Eu^{3+} ions at C_2 sites of cubic Y_2O_3 contains both odd and even CF terms and, therefore, magnetic- and electric-dipole transitions are both allowed. However, for Eu^{3+} ions at S_6 sites, which have a center of inversion, the CF Hamiltonian contains only even terms and only magnetic- and vibronic-coupled electric dipole transitions can be expected [67]. Thus nearly all the Eu^{3+} emission transitions are originated in only one of the two sites available for the Eu^{3+} ion; i.e., the C_2 site.

3.3.1. Broadband excitation

The electronic energy level scheme of the Eu^{3+} ions in solids consists of seven ^7F_J (J=0−6) multiplets well separated (around 12000 cm^{-1}) from the ^5D_J (J=0−4) ones and other strongly overlapped excited multiplets above the $^5D_3$ state at around 25000 cm^{-1} [31-33] The luminescence takes place mainly in the visible range between the multiplets of the low-energy terms, ^7F and ^5D. Fig. 5 shows the room temperature emission spectra of the Eu^{3+}-doped Y_2O_3 nanophosphors with sizes of 6 and 37 nm obtained under broadband excitation of the $^7F_0\rightarrow{}^5L_6$ transition at around 395 nm (25316 cm^{-1}). Note that when Eu^{3+} ions are excited to levels above the $^5D_0$ state there is a fast non-radiative multiphonon relaxation to this level because of the small energy difference between all the involve levels. However, Eu^{3+} ions decay radiatively from the $^5D_0$ level because the large energy difference to the closest $^7F_6$ level prevents the possibility of multiphonon relaxation. Therefore, the quantum emission efficiency of $^5D_0\rightarrow{}^7F_J$ transitions is close to the unity.

Different peaks corresponding to the $^5D_0\rightarrow{}^7F_J$ (J=0−4) transitions can be observed in Fig. 5. The $^5D_0\rightarrow{}^7F_1$ (585-605 nm) transition shows magnetic-dipole character and is allowed by all the selection rules independently on the composition of the host matrix [68-70]. The $^5D_0\rightarrow{}^7F_2$ (608−635 nm) and $^5D_0\rightarrow{}^7F_4$ (685−720 nm) transitions are electric-dipole in nature and are forced by the odd CF Hamiltonian. The $^5D_0\rightarrow{}^7F_J$ (J=0,3,5) emission transitions are strictly forbidden in the frame of the intermediate scheme of the Judd– Ofelt theory [71, 72], i.e. they do not obey the selection rules for the forced electric-dipole transitions: if the initial or final state is a singlet (J=0) then |ΔJ| = 2,4,6. Therefore, the low intensities of the $^5D_0 \rightarrow ^7F_0$ (around 580 nm) and $^5D_0 \rightarrow ^7F_3$ (640−675 nm) transitions of Eu^{3+} in cubic Y_2O_3 can be explained by the J-mixing effect, i.e. the mixing of wave functions of a given J-Stark state with those of the closer J multiplet states through the B_{2q}, B_{4q} and B_{6q} even CF parameters. This process induces an effective borrowing of intensity from the other electric-dipole transitions [73-75], especially from the high intense $^5D_0 \rightarrow ^7F_2$ hypersensitive transition.

According to group theory, the degeneracy of all the levels of Eu^{3+} ions at the low-symmetry C_2 site is completely lifted, giving rise to a number of Stark levels equal to 2J+1=1,3,5,7,9 with with angular momentum J=0,1,2,3,4 respectively. Since the $^5D_0$ initial emitting level is non-degenerate, the emission bands show a structure due CF splitting of the ^7F_J (J=1–4) levels. Thus, a complete identification of the number and energy positions of the ^7F_J Stark components have been obtained from the peak energies, which completely fit the energy levels observed at the C_2 site in Y_2O_3:Eu^{3+} cubic single crystal [10, 76, 77]. For comparison, the peak energy positions of the Eu^{3+} ions in bulk Y_2O_3 single crystal have been indicated by vertical lines in Fig. 5 [77]. It is worth noting that this identification is valid independently of the size of the nanophosphor, since no additional peaks, which could be related to other phases, have been observed in any of the nanophosphors, except for the weak peak at around 582.4 nm that will be discussed later. Thus, it can be concluded from luminescence measurements that, with the present method of synthesis, a cubic structure has been obtained for all the Y_2O_3 nanophosphors, independently of the annealing temperature. This conclusion is in agreement with the XRD and Raman scattering measurements previously discussed.

Important differences in the linewidths of the emission peaks are observed for nanocrystals with different sizes (see Fig. 5 and the inset). All the emission peaks show a large broadening for the smallest nanophosphors (6 nm), which is especially evident when comparing the $^5D_0 \rightarrow ^7F_{3,4}$ emissions. With the increase of the annealing temperature and the size of the nanoparticles, the emission bands become more defined and sharper, resulting in a spectrum quite similar to that measured in a Y_2O_3 single crystal. These results indicate that: i) all Eu^{3+} ions occupy the same crystallographic position (C_2 site) in the core of the nanophosphors, which is the same as in the bulk material, and named hereafter as the 'true' C_2 site and, ii) in the smallest nanophosphors there is an inhomogeneous broadening of the emission profiles due to the existence of a continuous distribution of C_2 environments for the Eu^{3+} ions related to distortions, or relaxations, of the yttria structure closer to the surface of the nanoparticles in which a higher segregation of Eu^{3+} ions to the surface occurs. It is evident that higher annealing temperatures favor the generation of a nanomaterial with cubic structure of better crystallinity and homogeneous location of Eu^{3+} ions in 'true' C_2 sites as the nanophosphor size increases. A similar behavior can be assumed for those Eu^{3+} ions located at the S_6 sites (observed in electronic Raman scattering) as the nanocrystal size increases.

3.3.2. Time-resolved site-selective spectroscopy

To obtain more information about the inhomogeneous broadening of the emission bands in the smallest nanocrystals, the $^7F_0 \leftrightarrow ^5D_0$ transitions between singlet (non-degenerate) levels have been analysed in detail. These transitions give single peaks that cannot be splitted by any local point symmetry (crystal-field) around the Eu^{3+} ion. Consequently, any additional peak observed for these transitions should be directly related to other available Eu^{3+} sites in the nanophosphors of the cubic phase or another one, either crystalline or amorphous.

The $^5D_0 \rightarrow ^7F_0$ and $^5D_0 \rightarrow ^7F_1$ transitions for four different nanophosphors are shown in the inset of Fig. 5. It can be clearly observed that there is a broadband contribution to the short-wavelength side of the $^7F_0 \rightarrow ^5D_0$ transition for the smallest nanophosphors (those annealed at 500 and 600 ºC). This broadband overlaps with the single peak associated to Eu^{3+} ions in the 'true' C_2 site at 581.2 nm and also with the peak associated to Eu^{3+} ions in an second phase at around 582.4 nm, which is present in all Eu^{3+}-doped nanophosphors.

We have performed time-resolved excitation spectra associated to the $^7F_0 \rightarrow ^5D_0$ transition in the smallest Eu^{3+}-doped nanoparticles (6 nm) and obtained by detecting the $^5D_0 \rightarrow ^7F_1$ transition at 13 K under a pulsed laser excitation (Fig. 6). A broadband detection at 593 nm has been chosen since a contribution from all the environments and sites of the Eu^{3+} ions to this emission is expected. The spectra are presented normalized to the emission of the Eu^{3+} ions in the 'true' C_2 site at 581.2 nm. The spectrum taken 30 μs after the laser pulse resembles that of the steady state emission spectrum of Fig. 5 except that the peak at 582.4 nm is completely masked by the emission of the Eu^{3+} ions in the 'true' C_2 site. The large broadband contribution to the short-wavelength side of this single peak is due to the overlapping of homogeneous $^5D_0 \rightarrow ^7F_0$ spectra of Eu^{3+} ions located at different environments or sites in the nanophosphor. Therefore, many emissions have slightly different energies than those Eu^{3+} ions in the 'true' C_2 site. Increasing the time delay after the laser pulse results in a faster decay of the emissions from these environments compared to the emission of Eu^{3+} ions in the 'true' C_2 site. Furthermore, both emissions decay much faster than the emission of the second phase, which can be seen with an increasing intensity with the time delay respect to the 'true' C_2 site.

To interpret these results it must be recalled that XAS measurements of Qi *et al.* observed an increase of structural disorder in Y_2O_3:Eu^{3+} nanophosphors on decreasing size from 40 to 9 nm [16]. They concluded that Eu^{3+} and Y^{3+} ions located near the surface of the nanoparticles had a higher coordination than those far from the surface and this result was observed for the two phases coexisting in the nanoparticles: one crystalline $Y_2O_3:Eu^{3+}$ and one amorphous unknown phase. In this context, Song *et al.* [78], suggested that the proportion of surface atoms in $Y_2O_3:Eu^{3+}$ nanocrystals is quite high (about 80% for ~5 nm particles) compared to bulk sample (less than 1% for ~3 mm sample), thus enhancing the proportion of local displacement and making the near surface of the nanosized particle particularly unstable. Moreover, an amorphous phase has been also observed in several works reporting monoclinic and cubic Y_2O_3 nanophosphors, where it has been suggested that they could be due to faceting between nanoparticles, necks between particles, the presence of adsorbates or particularities in the chemistry of the particle´s surface [20, 43, 44].

On the basis of the above arguments, we tentatively attribute the broadband contribution in the smallest nanoparticles to Eu^{3+} ions in a distribution of environments with an increasing fluctuation of their local structures due to differences in the Eu^{3+}-ligand bond distances and angles when reaching the surface of the nanoparticle. In fact, since the broad shoulder appears at the short-wavelength side of the $^7F_0 \rightarrow ^5D_0$ excitation we can assume that this broadband is associated to Eu^{3+} ions located in environments that feel stronger CF interactions with their ligands. Thus, in 6-nm-size nanophosphors, there would be a large dispersion of environments for the nanostructures with distorted cubic structure leading to stronger CF than those present in the 'true' C_2 cubic sites (observed in the nanostructures with larger sizes) of the bulk material. In other words, the 'true' cubic C_2 site would act as a 'parent structure' that, after suitable distortions, would give rise to all the distribution of environments for the Eu^{3+} ions present in the smallest nanophosphors. This hypothesis is supported by the strain and the large increase of the lattice parameter that we have measured in the smallest nanocrystals. These two facts allow a large proportion of Eu^{3+} ions to reside in distorted environments of the 'true' C_2 and S_6 sites of the cubic structure, a hypothesis coherent with the large segregation of Eu^{3+} ions to the surface in the smallest nanophosphor. Note that in the largest nanocrystals studied (37 nm size) there is a negligible strain and the lattice parameter is similar to that of the bulk Y_2O_3 single crystal; thus, all Eu^{3+} ions reside in 'true' C_2 and S_6 sites.

The existence of a variety of local structures in our smallest nanophosphors becomes evident after exciting selectively with laser light within the $^7F_0 \rightarrow ^5D_0$ excitation profile. Fig. 7 presents the time-resolved site-selective spectroscopy (FLN) emission spectra of the $^5D_0 \rightarrow ^7F_1$ transition exciting selectively the high-energy side of the $^7F_0 \rightarrow ^5D_0$ band. Differences in the local sites of the Eu^{3+} ions in the nanophosphor are clearly reflected in the number of peaks and the emission wavelengths of the transitions to the three $^7F_1$ Stark levels, especially for the emission to the $^7F_1$ lowest energy Stark component that shows a large sensitivity with the laser excitation [33-35]. As shown in Fig. 7, three peaks are observed for the $^5D_0 \rightarrow ^7F_1$ transition after the excitation of Eu^{3+} ions at 581.2 nm. They confirm the existence of a low symmetry and weak CF acting on Eu^{3+} ions in the 'true' C_2 site. However, when exciting at lower wavelengths in the range from 578 to 580.4 nm within the inhomogeneous broadband contribution, some extra peaks are observed at around 587.4 and 596 nm. These extra peaks could be ascribed to emissions of the Eu^{3+} ions both at the C_2 sites, for the peak at 587.4 nm, and at the second site, for the peak at 596 nm, after a simultaneous laser excitation or due to energy transfer processes between Eu^{3+} ions at different sites or environments [79].

In order to selectively excite the second site, the FLN technique has been applied within the $^7F_0 \rightarrow ^5D_1$ transition exciting at 527 nm at 13 K and its emission spectrum is shown in Fig. 7. Apart from the emission peak at 582.4 nm, there is a structured emission in the 592−597 nm range that can be correlated with the extra peak at around 596 nm observed in the emission under selective excitation at the short-wavelength side of the $^5D_0$ band. In this respect, Tissue and Yuan [44] have identified different contributions in the excitation spectrum of Eu^{3+} in 5-nm-size $Y_2O_3:Eu^{3+}$ nanophosphors due to the coexistence of phases: the cubic Y_2O_3 structure, the monoclinic $Eu^{3+}:Y_2O_3$, and the monoclinic Eu_2O_3. Since Eu^{3+} ions in the monoclinic nanostructures may occupy three different sites (A,B,C) [44, 80], three relatively broad emission peaks should be observed for the $^5D_0 \rightarrow ^7F_0$ transition at around 578.5−579, 582.2 and 582.4 nm in the smallest nanoparticles [81]. After annealing, those peaks should become narrow at around 578.5, 582.2 and 582.4 nm for monoclinic Eu_2O_3 and slightly shifted at 579.2, 582.6 and 582.89 nm for monoclinic $Y_2O_3:Eu^{3+}$ [44]. Similarly, Jang et al. have shown by site-selective spectroscopy that new peaks appear in the excitation spectra of the $^7F_0 \rightarrow ^5D_0$ transition in cubic $Y_{2-x}Gd_xO_3:Eu^{3+}$ when a monoclinic structure is developed on increasing Gd content [82], being the most prominent peaks due to Eu^{3+} emission those of the B and C sites which are located around 582.02 nm, while the peak corresponding to the A site (located around 578.65 nm) is of smaller intensity. It is noteworthy that only the broad band around 582.4 nm is observed in the steady state luminescence of our nanophosphors (Fig. 5) what could be consistent with the residual presence of the monoclinic phase in our samples (not observed by XRD and Raman measurements) despite the lifetimes of this secondary phase (9 ms) are larger than those in monoclinic Eu_2O_3 nanophosphors (a few hundreds of microseconds) and than those in monoclinic $Y_2O_3:Eu^{3+}$ (1-2 ms) according to Ref. 83. In this respect, the larger lifetime measured in our nanophosphors could be related to the presence of trap centers in the monoclinic phase. However, the possibility that emissions different from those of the Eu^{3+} ions at C_2 sites could belong to the $^5D_0 \rightarrow ^7F_1$ magnetic dipole–allowed emissions of Eu^{3+} ions at S_6 sites cannot be disregarded [84].

3.3.3. Crystal-field analysis

Since the CF strength experienced by the Eu^{3+} ions is a measure of their electrostatic interaction with the surrounding O^{2-}, the higher CF strength present in the surface of the nanophosphors must be due to the larger charge density and/or to a smaller Eu-O distance near the surface. The higher coordination of the Eu^{3+} ions in the smallest nanophosphors found by XAS measurements [16] lead us to think that the cause of the larger CF near the surface of the smallest nanocrystals must be due to a larger charge density around Eu ions near the nanocrystal surface since a higher coordination of Eu^{3+} ions is usually related to larger Eu-O distances, what in fact is in agreement with the increase of the lattice parameter as the nanocrystal size decreases**.**

The average strength of the CF acting on the Eu^{3+} ions in Y_2O_3:Eu^{3+} nanophosphors can be estimated from the splitting of the $^7F_1$ multiplets into three Stark levels. From the FLN measurements, the positions of the $^7F_1$ Stark levels with respect to $^7F_0$ ground level are collected and plotted as a function of excitation wavelength in the inset of Fig. 8. In a first approximation, if the J-mixing is neglected, only the second rank real CF parameters, B_{20} and B_{22}, of the even CF Hamiltonian will affect significantly to the breakdown of the degeneracy of the $^7F_1$ term into three Stark levels [66, 70, 79]. Due to the almost symmetrical splitting observed for the three $^7F_1$ Stark levels with the CF increase, the B_{22} parameter should exhibit a large variation in magnitude, while the B_{20} axial parameter should be rather low and will not affect significantly to the splitting [66, 85]. Auzel and Malta [86] have tried to simplify the CF description defining a scalar, rotational invariant parameter called the CF strength that, for the C_2 local symmetry, takes the form

$$N_V(B_q^2) = \sqrt{\left(\frac{4\pi}{2k+1}\right)\ \left(|B_{20}|^2 + 2|B_{22}|^2\right)} \qquad (1)$$

that can be also easily related to the maximum splitting of the $^7F_1$ level, [87]

$$N_V(B_{2q}) = \sqrt{\frac{2 + \left(\frac{E_b - E_c}{\Delta E_{MAX}/2}\right)^2}{0.3/\pi}}\ \Delta E_{MAX}(^7F_1) \tag{2}$$

where E_b is the barycentre of energy of the $^7F_1$ level, calculated as the mean energy of the corresponding three Stark levels, whereas E_C is the energy of the central Stark level.

The second rank CF strength parameter $N_V(B_{2q})$ is shown in Fig. 8 as a function of the experimental maximum splitting of the $^7F_1$ manifold, $\Delta E_{MAX}(^7F_1)$, obtained from the $^7F_1$ splitting shown in the inset. Its value is larger than those usually found in glasses [33, 35, 70, 79, 84]. Furthermore, the almost symmetrical splitting of the $^7F_1$ Stark levels observed in $Y_2O_3:Eu^{3+}$ gives rise to an almost constant factor between the CF strength and the maximum splitting of the $^7F_1$ level of 0.218 for all the environments, giving rise to the linear dependence shown in Fig. 8, as predicted by Malta *et al.* [87].

A different perspective is obtained if the J-mixing is taken into account. Görller-Walrand and Binnemans [66] have re-defined the ‘weak CF’ (J-mixing negligible) and ‘strong CF’ (J-mixing unnegligible) for the RE^{3+}-doped systems. According to this definition a distribution of environments under weak-medium ($300 < \Delta E_{MAX}(^7F_1) < 450$ cm^{-1}) and strong ($\Delta E_{MAX}(^7F_1) > 450$ cm^{-1}) CFs can be obtained for our nanophosphors. If a structural model dares to explain the inhomogeneous distribution of Eu^{3+} environments it has to take into account that: i) the weakest CF environment for the Eu^{3+} ion is that at the 'true' C_2 cubic site, and ii) there are no sharp changes in both the emission intensities and the $^7F_1$ splitting when moving the excitation to stronger CF environments to the high-energy side of the $^5D_0$ band profile. Under this viewpoint, it is possible to understand the continuous distribution of environments for the Eu^{3+} ions in the smallest nanophosphors as a continuous distortion of the 'true' C_2 site of the cubic Y_2O_3 structure as Eu^{3+} ions get closer to the nanocrystal surface. In this sense, stronger CF environments are obtained by successive distortion of the C_2 site parallel to the increase of the CF strength, which give rise to larger splitting of the multiplets as the nanocrystal size decreases. We can speculate that in the smallest nanophosphors, as those with 6 nm size, the presence of dangling bonds at the surface can contribute significantly to the local distortion of the large proportion of Eu^{3+} ions near the surface.

To finish we would like to stress that our hypothesis of the continuous distortion of the C_2 sites suggested by site-selective excitation is supported by the absence of extra peaks associated to secondary phases in the XRD pattern, in the Raman spectrum, and in the steady-state Eu^{3+} luminescence of our smallest nanophosphors. Furthermore, it is consistent with XAS measurements that evidence a larger structural disorder, leading to drastic changes in the local structure, as Y_2O_3 nanoparticles become smaller [16]. In this way, Eu^{3+} ions closer to the surface of the cubic Y_2O_3 nanoparticles would have a coordination closer to 9 (in the distorted C_2 sites) than to 6 (in the 'true' C_2 sites), and the increase in coordination would explain the stronger CF felt by Eu^{3+} ions near the surface than in the core. Note that the above explanation is different to that Qi *et al.* [16] who related the disorder to the existence of an amorphous phase coexisting with the 'true' C_2 site, instead of consider this site as the 'parent structure' for the Eu^{3+} environments in the small nanophosphors.

4. Conclusions

Undoped and Eu^{3+}-doped cubic yttria nanoparticles with considerable good crystallinity have been synthesized by means of a complex-based precursor solution method. Depending upon the temperature of the annealing treatment, nanophosphors with sizes between 6 and 37 nm, all showing narrow size distributions, have been obtained. No amorphous or secondary phases, like monoclinic Y_2O_3 or Eu_2O_3, have been detected in the nanocrystals. While nanoparticles of 37 nm have similar lattice parameters than bulk cubic yttria, the lattice parameter in the nanoparticles increases up to 0.26% (in undoped Y_2O_3) and

0.33% (in Eu^{3+}-doped Y_2O_3) as the particle size decreases from 37 to 6 nm. Raman scattering spectra of Eu^{3+}-doped nanoparticles have shown four more bands than undoped nanoparticles. The origin of three of them is unknown, but one clearly corresponds to electronic Raman scattering originated from Eu^{3+} ions in S_6 sites, which confirms that Eu^{3+} ions substitute Y^{3+} ions in both C_2 and S_6 sites of the cubic structure.

Size-dependent photoluminescence emission spectra have been measured in Y_2O_3:Eu^{3+} nanoparticles. In 37 nm-sized samples, emissions are similar to bulk yttria in which Eu^{3+} ions are located preferentially in the cubic C_2 sites. However, in 6 nm-size samples, the ${}^5D_0 \rightarrow {}^7F_0$ transition consists of a high-energy broadband contribution overlapped with two sharp peaks. The sharp peaks of the ${}^5D_0 \rightarrow {}^7F_0$ transition should correspond to crystalline phases within the core of the nanophosphors. One of them is due to Eu^{3+} in the C_2 cubic site of Y_2O_3 nanophosphor and the other could be tentatively assigned to a residual monoclinic structure of Y_2O_3 present in the nanocrystals. Therefore, it is possible that they belong to ${}^5D_0 \rightarrow {}^7F_1$ magnetic-dipole allowed emission of Eu^{3+} ions at S_6 sites. Finally, site-selective excitation in the ${}^7F_0 \rightarrow {}^5D_0$ peaks has allowed us to associate the broadband contribution to a continuous distortion of the C_2 site caused by a large disorder, especially near the surface, found in the smallest nanophosphors.

Acknowledgements

Authors are grateful to Ministerio de Ciencia e Innovación of Spain (MICINN) under The National Program of Materials (MAT2010-21270-C04-02/03/04), the Consolider-Ingenio 2010 Program (MALTA CSD2007-0045), Generalitat Valenciana (GVA-ACOMP-2013-012), and to the EU-FEDER funds for their financial support. F.J.M. and O.G. are grateful to the Vicerrectorado de Investigación y Desarrollo of the Universitat Politècnica de València (UPV2011-0914 PAID-05-11 and UPV2011-0966 PAID-06-11). S.F.L-L. wishes to thank

MICCIN for a FPI grant (BES-2008-003353). Finally, S.R. wishes to thank Universitat Politècnica de València and Universidad de La Laguna for the financial support during her research stays.

References

[1] T. Igarashi, M. Ihara, T. Kusunoki, K. Ohno, T. Isobe, M. Senna, Appl. Phys. Lett. 76 (2000**)** 1549.

[2] A.N. Jennifer, L.B. Edward, M. J. Wagner, Chem. Mater. 15 (2003) 688.

[3] R. Reisfel and C.K. Jorgensen, *Lasers and Excited States of Rare Earths* (Berlin Springer: 1977).

[4] F.X. Gan, *Optical and Spectroscopic Properties of Glass,* (Berlin: Springer 1992).

[5] B.M.J. Smets, Materials Chemistry and Physics 16 (1987) 283.

[6] S. Tanabe, J. Non-Cryst. Solids 259 (1999) 1.

[7] A.J. Kenyon, Progress in Quantum Electronics 26 (2002)225.

[8] P.N. Prasad, *Nanophotonics,* (John Wiley & Sons: NY, 2004).

[9] N. Yamada, S. Shionoya, T. Kushida, J. Phys. Soc. Jpn. 32 (1972) 1577.

[10] C.A. Morrison and R.P. Leavitt*, Spectroscopic Properties of Triply Ionized Lanthanides in Transparent Host Crystals, in Handbook of the Physics and Chemistry of Rare Earths*, (edited by K. A. Gschneidner, Jr. and L. Eyring, Elsevier Science Publisher 1982).

11] D. S. Lee , A.J. Steckl, Appl. Phys. Lett. 81(2002) 2331.

[12] R.N. Bhargava, J. Lumin. 70 (1996) 85.

[13] G. Blasse, B.C. Grabmaier, *Luminescent Materials* [Springer Berlin: 1994].

[14] N.C. Chang, K.A. Wickersheim, R.A. Lefever, R.L White, Meeting of American Physical Society (Stanford, 1962); N.C. Chang, J. Appl. Phys. 34 (1963) 3500.

[15] A. Konrad, T. Fries, A. Gahn, F. Kummer, U. Herr, R. Tidecks, K. Samwer, J. Appl. Phys. 86 (1999) 3129.

[16] Z. Qi, C. Shi, W. Zhang, W. Zhang, T. Hu, Appl. Phys. Lett. 81 (2002) 2857.

[17] W.W. Zhang, W.P. Zhang, P.B. Xie, M. Yin, H.T. Chen, L. Jing, Y.S. Zhang, L.R. Lou, S.D. Xia, J. Colloid. Interface Sci. 262 (2003) 588.

[18] S. Ray, P. Pramanik, A. Sinha, A. Roy, J. Appl. Phys. 97 (2005) 094312.

19] Y. Repelin, C. Proust, E. Husson, J.M. Beny, J. Solid State Chem. 118 (1995) 163.

[20] H. Eilers, B.M. Tissue, Chem. Phys. Lett. 251 (1996) 74.

[21] W.W. Zhang, M. Xu, W.P. Zhang, M. Yin, Z.M. Qi, S.D. Xia, C. Garapon, Chem. Phys. Lett. 376 (2003) 318.

[22] Q.L. Dai, M.E. Foley, Ch. J. Breshike, A. Lita, G.F. Strouse, J. Am. Chem. Soc. 133 (2011) 15475.

[23] B.G. Wybourne, *Spectroscopic Properties of Rare Earths*, (Wiley-Interscience, New York, 1965).

[24] G. De, W. Qin, J. Zhang, Y. Zhang, Y. Wang, C. Cao, Y. Cui, J. Lumin. 119−120 (2006) 258.

[25] A. Mehta, T. Thundat, M.D. Barnes, V. Chhabra, R. Bhargava, A.P. Bartko, R.M. Dickson, Appl. Opt. 42 (2003) 2132.

[26] J.W. Stouwdam, C. J. Van Veggel, Nano Lett. 2 (2002) 733.

[27] H. Schniepp, V. Soghdar, Phys. Rev. Lett. 89 (2002) 257403.

[28] R.S. Meltze, S.P. Feofilov, B. Tissue, H. B. Yuan, Phys. Rev. B 60 (1999) R14012.

[29] P. Ghosh, A. Patra, J. Nanosci. Nanotech. 8 (2008)1.

[30] S. Sadhu, T. Sen, A. Patra, Chem. Phys. Lett. 440 (2007) 121.

[31] W.M. Yen, P.M. Selzer, *Laser Spectroscopy of Solids* (Springer-Verlag, Berlín, 1986).

[32] G.F. Imbusch, Physica Scripta T 19 (1987) 354.

[33] V. Lavín, P. Babu, C.K. Jayasankar, I.R.Martín, V.D. Rodríguez, J. Chem. Phys. 115 (2001) 10935.

[34] V. Lavín, V.D. Rodríguez, I.R. Martín, U.R. Rodríguez-Mendoza, J. Lumin. 72-74, (1997) 437.

[35] P. Babu, K.H. Jang, E.S. Kim, R. Vijaya, C.K. Jayasankar, V. Lavín, H.J. Seo, J. Non-Cryst. Solids 357 (2011) 2139.

[36] K. Zhang, A.K. Pradhan, G.B. Loutts, U.N. Roy, Y. Cui, A. Burger, J. Opt. Soc. Am. B 21 (2004) 1804.

[37] A. Mujica, A. Rubio, A. Muñoz, R.J. Needs, Rev. Mod. Phys. 79 (2003) 863.

[38] G. Kresse, J. Hafner, Phys. Rev. B 47 (1993) 558 ibid, 49 (1994)14251; G. Kresse, J. Furthmüller, Comput. Mat. Sci. 6 (1996) 15; G. Kresse, J. Furthmüller, Phys. Rev. B 54 (1996) 11169.

[39] P. Hohenberg, W. Kohn, Phys. Rev. 136 (1964) 3864.

[40] P.E. Blöchl, Phys. Rev. B 50 (1994) 17953. G. Kresse, D. Joubert, Phys. Rev. B 59 (1999) 1758.

[41] J.P. Perdew, A. Ruzsinszky, G.I. Csonka, O.A. Vydrow, G.E. Suseria, L.A. Constantin, X. Zhou, K. Burke, Phys. Rev. Lett. 100 (2008) 136406.

[42] K. Parlinski, computer code PHONON. See: http://www.computingformaterials.com/index.html.

[43] D.K. Williams, B. Bihari, B.M. Tissue, J. M. McHale, J. Phys. Chem. B 102 (1998) 916.

[44] B.M. Tissue, H.B. Yuan, J. Solid State Chem. 171 (2003) 12.

[45] L. Wang, Y.X. Pan, Y. Ding, W. Yang, W.L. Mao, S.V. Sinogeikin, Y. Meng, G.Y. Shen, H.K. Mao, Appl. Phys. Lett. 94 (2009) 061921.

[46] C. Beck, K.-H. Ehses, R. Hempelmann, Ch. Bruch, Scripta Mater. 44 (2001) 2127.

[47] M.I. Arroyo, J.M. Perez-Mato, C. Capillas, E. Kroumova, S. Ivantchev, G. Madariaga, A. Kirov, H. Wondratschek, Z. Krist. 221 (2006) 15.

[48] Ch. Beck, Ch. Bruch, K. -H. Ehses, R. Hempelmann, J. Phys. IV France 10 (2000) 87.

[49] J.E. Spanier, R.D. Robinson, F. Zhang, S.W. Chan, I.P. Herman, Phys. Rev. B 64 (2001) 245407.

[50] E. Husson, C. Proust, P. Gillet, J. P. Itie, Mat. Res. Bull. 34 (1999) 2085.

[51] A. Ubaldini, M.M. Carnasciali, J. Alloys & Comp. 454 (2008) 374.

[52] J. Lancok, C. Garapon, C. Martinet, J. Mugnier, R. Brenier, Appl. Phys. A 79 (2004) 1263.

[53] A. Kremenovic, J. Blanusa, B. Antic, Ph. Colomban, V. Kahlenberg, C. Jovalekic, J. Dukic, Nanotechnology 18 (2007) 145616.

[54] N. Dilawar, S. Mehrotra, D. Varandani, B.V. Kumaraswamy, S. K. Haldar, A. K. Bandyopadhyay, Mater. Charact. 59 (2008) 462.

[55] J. F. Martel, S. Jandl, B. Viana, D. Vivien, J. Phys. Ceram. Solids 61 (2000) 1455.

[56] M. Jayasimhadri, B. V. Ratnam, K.W. Jang, H. S. Lee, B. J. Chen, S. -S. Yi, J. -H. Jeong, L. Rama Moorthy, J. Am. Ceram. Soc. 93 (2010) 494.

[57] Q. Lü, Y. J. Wu, A. H. Li, Y. Wang, Y. Gao, H. Y. Peng, Mater. Sci. Eng. B 176 (2011) 1041.

[58] S. Saengkerdsub, H. -J. Im, C. Willis, S. Dai, J. Mater. Chem. 14 (2004) 1207.

[59] W. W. Zhang, W. P. Zhang, P. B. Xie, M. Yin, H. T. Chen, L. Jing, Y. S. Zhang, L. R. Lou, S. D. Xia, J. Colloid Inter. Sci. 262 (2003) 588.

[60] J. A. Koningstein, J. Chem. Phys. 42 (1965) 3195.

[61] J. A. Koningstein, O. S. Mortensen, Phys. Rev. Lett. 18 (1967) 831.

[62] G. Schaack, J. A. Koningstein, J. Opt. Soc. Am. 60 (1970) 1110.

[63] G. S. Nolas, V. G. Tsoukala, S. K. Gayen, G. A. Slack, Phys. Rev. B 50 (1994) 150; idem, Opt. Lett. 19 (1994) 1574.

[64] J. Heber, K. H. Hellwege, U. Köbler, H. Murmann, Z. Phys. 237 (1970) 189.

[65] J. B. Gruber, R. P. Leavitt, C. A. Morrison, N. C. Chang, J. Chem. Phys. 82 (1985) 5373.

[66] C. Görller-Walrand, K. Binnemans, *Rationalization of Crystal-Field Parametrization" in "Handbook on the Physics and Chemistry of Rare Earths* (North-Holland Publishing Co., p. 121, 1996).

[67] G. Blasse, Inorg. Chim. Acta 167 (1990) 33.

[68] R. D. Peacock, Structure and Bonding 22 (1975) 83.

[69] E. W. L. J. Oomen, A. M. A. Van Dongen, J. Non-Cryst. Solids 111 (1989) 206.

[70] V. Lavín, U. R. Rodríguez-Mendoza, I. R. Martín, V. D. Rodríguez, J. Non-Cryst. Solids 319 (2003) 200.

[71] B. R. Judd, Phys. Rev. 127 (1962) 750.

[72] G. S. Ofelt, J. Chem. Phys. 37 (1962) 511.

[73] G. Nishimura, T. Kushida, J. Phys. Soc. Japan 60 (1991) 683; Ibid., 60 (1991) 695.

[74] M. Tanaka, G. Nishimura, T. Kushida, Phys. Rev. B 49 (1994) 16917.

[75] V. Lavín, U.R. Rodríguez-Mendoza, I.R. Martín, V.D. Rodríguez, J. Non-Cryst. Solids 319 (2003) 200.

[76] N. C. Chang, J. B. Gruber, J. Chem. Phys. 41 (1964) 3227.

[77] J. Dexpert-Ghys, M. Faucher, Phys. Rev. B 20 (1979) 10.

[78] H. Song, B. Chen, H. Peng, J. Zhang, Appl. Phys. Lett. 81 (2002) 1776.

[79] J. E. Muñoz-Santiuste, U. R. Rodríguez-Mendoza, J. González-Platas, V. Lavín, J. Chem. Phys. **130** (2009) 154501.

[80] D. K. Williams, H.B. Yuan, B. M. Tissue, J. Lumin. 83-84 (1999) 297.

[81] B. M. Tissue, B. Bihari, J. Fluorescence 8 (1998) 289.

[82] K.H. Jang, E.S. Kim, J.S. Bae, S.S. Yi, J.H. Jeong, and H.J. Seo, Thin Solid Films 516 (2008) 5567.

[83] B. Bihari, H. Eilers, B. M. Tissue, J. Lumin. 75 (1997) 1.

[84] R. G. Pappalardo, R. B. Hunt Jr, J. Electrochem. Soc. 132 (1985) 721.

[85] J. Dexpert-Ghys M. Faucher, Phys. Rev. B 24 (1981) 3138.

[86] F. Auzel, O. L. Malta, J. Phys. (France) 44, 201 (1983).

[87] O. L. E. Malta, M. Antic-Fidancev, Lemaitre-Blaise, A. Milicic-Tang, M. Taibi, J. Alloys and Compd. 228 (1995) 41.

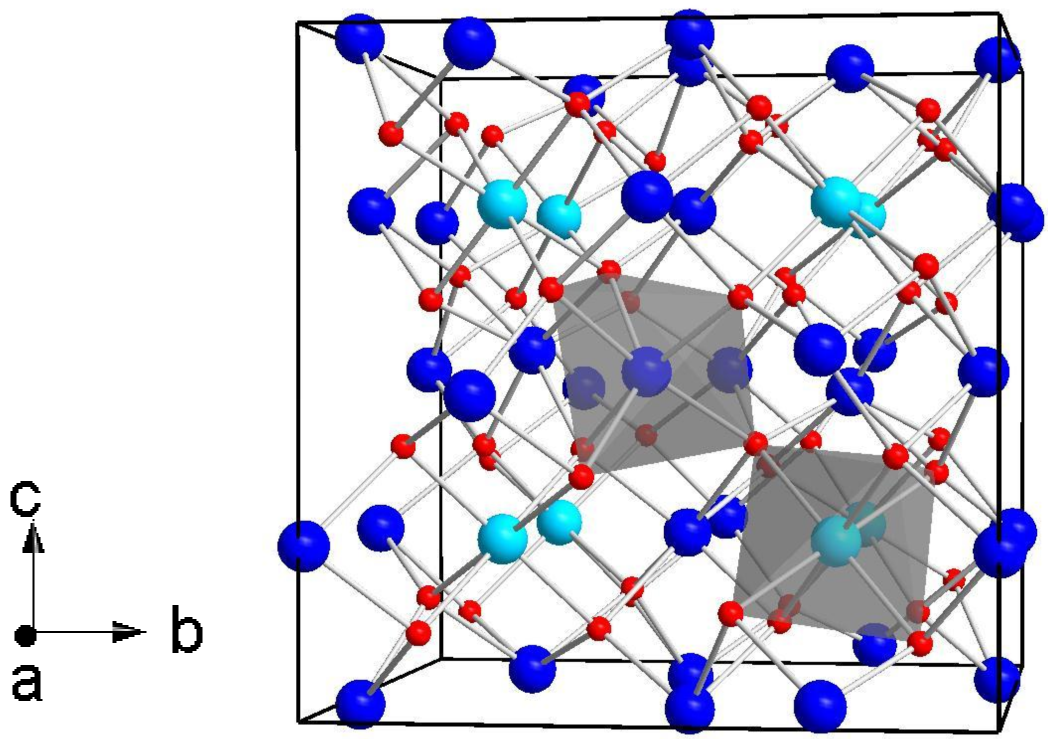

Fig. 1

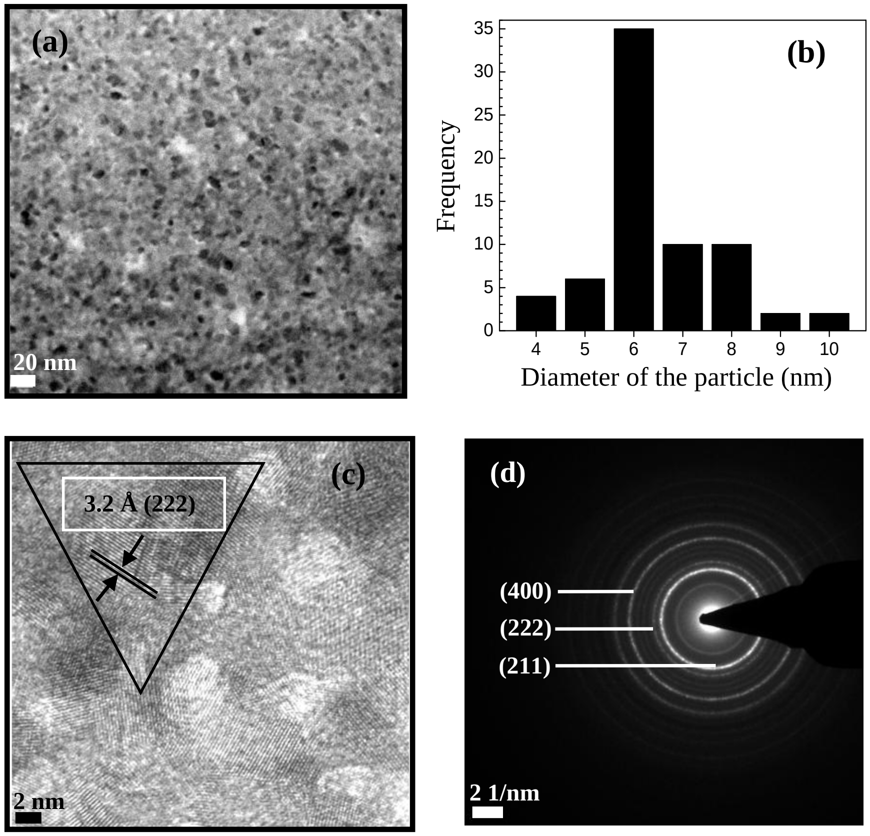

(a)
20 nm
(b)
Frequency
Diameter of the particle (nm)
0
5
10
15
20
25
30
35
4
5
6
7
8
9
10
(c)
3.2 Å (222)
2 nm
(d)
(400)
(222)
(211)
2 1/nm

Fig. 2

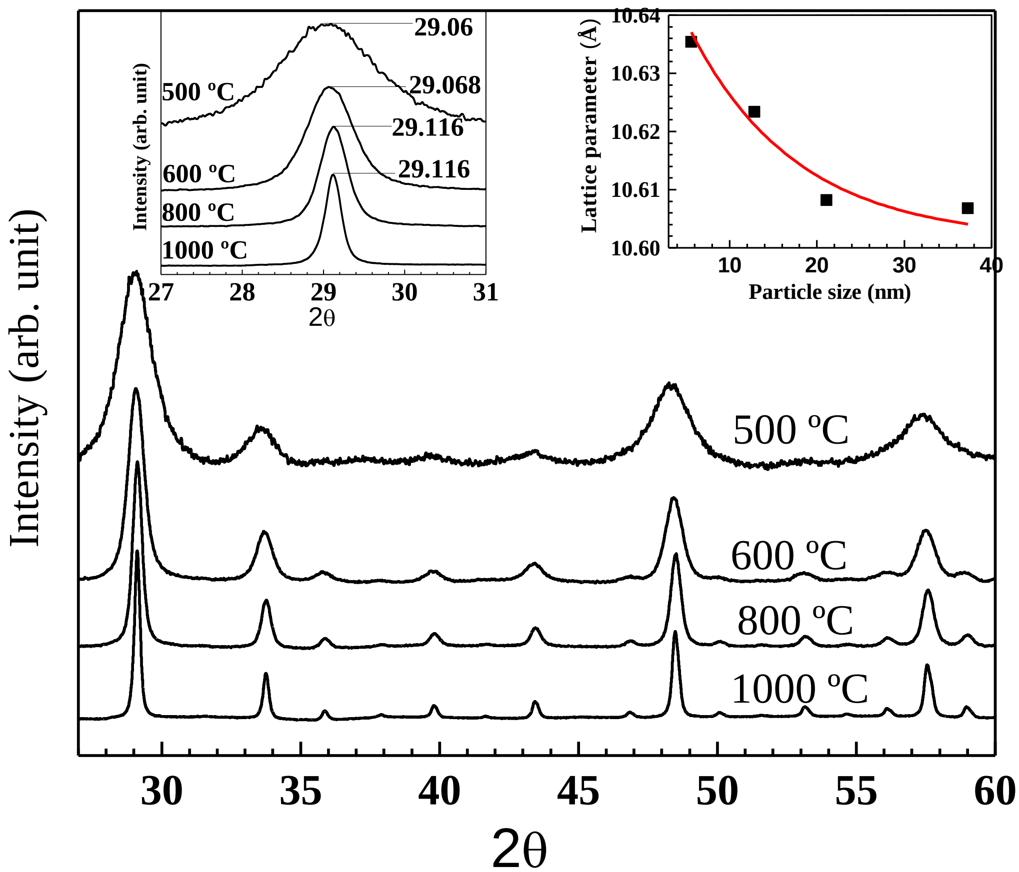
29.06
500 ºC
29.068
29.116
600 ºC
29.116
800 ºC
1000 ºC
Intensity (arb. unit)
27
28
29
30
31
2θ
10.64
10.63
10.62
10.61
10.60
Lattice parameter (Å)
10
20
30
40
Particle size (nm)
Intensity (arb. unit)
500 ºC
600 ºC
800 ºC
1000 ºC
30
35
40
45
50
55
60
2θ

Fig. 3

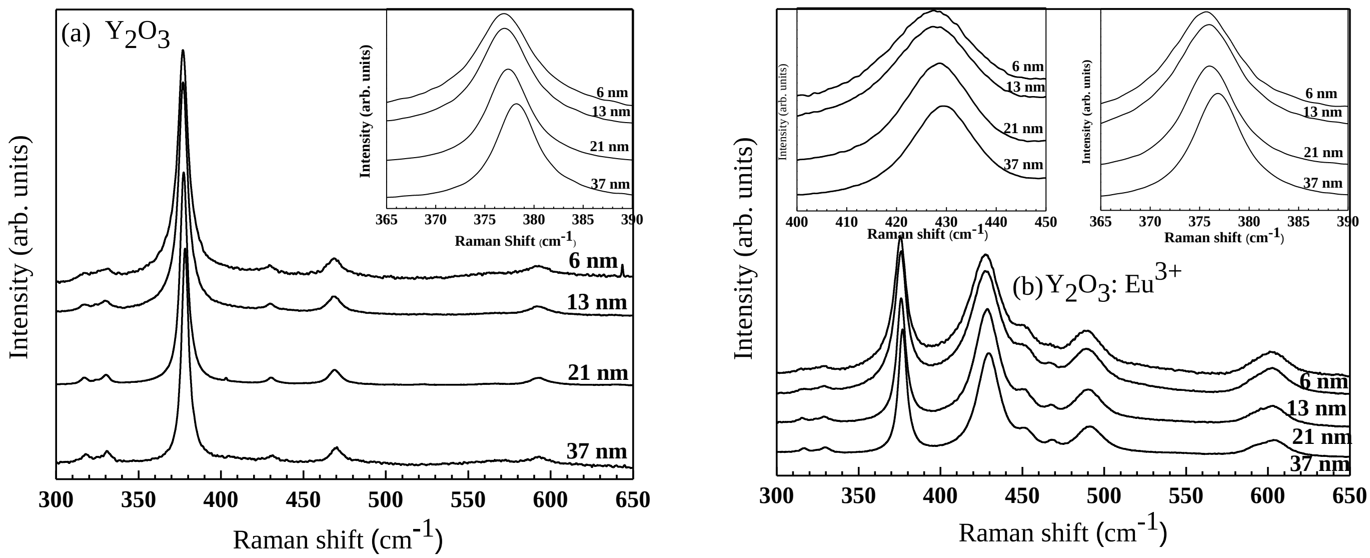
(a) Y_2O_3
Intensity (arb. units)
Raman shift (cm^{-1})
6 nm
13 nm
21 nm
37 nm
Raman Shift (cm^{-1})
(b) Y_2O_3: Eu^{3+}
Raman shift (cm^{-1})

Figs. 4

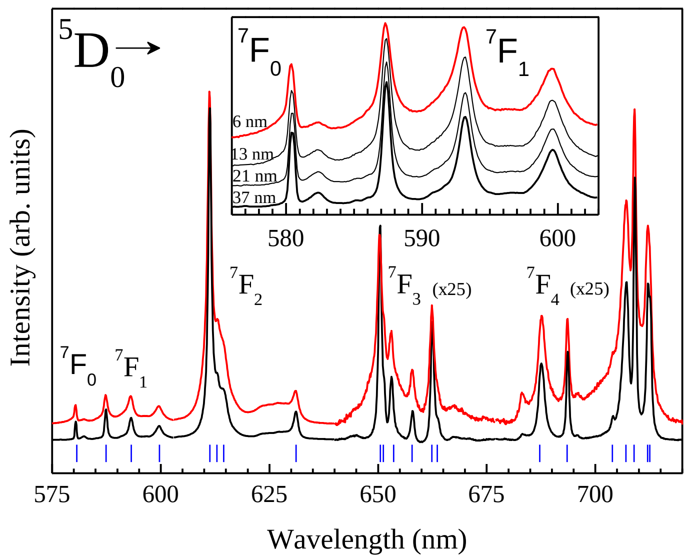

$^5D_0 \rightarrow$
$^7F_0$
$^7F_1$
$^7F_2$
$^7F_3$ (x25)
$^7F_4$ (x25)
6 nm
13 nm
21 nm
37 nm
580
590
600
575
600
625
650
675
700
Intensity (arb. units)
Wavelength (nm)

Fig. 5

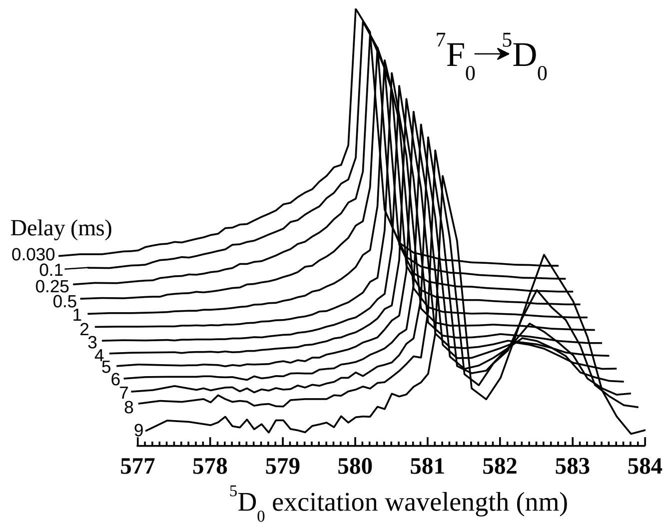

$^7F_0 \rightarrow {}^5D_0$
Delay (ms)
0.030
0.1
0.25
0.5
1
2
3
4
5
6
7
8
9
577
578
579
580
581
582
583
584
$^5D_0$ excitation wavelength (nm)

Fig. 6

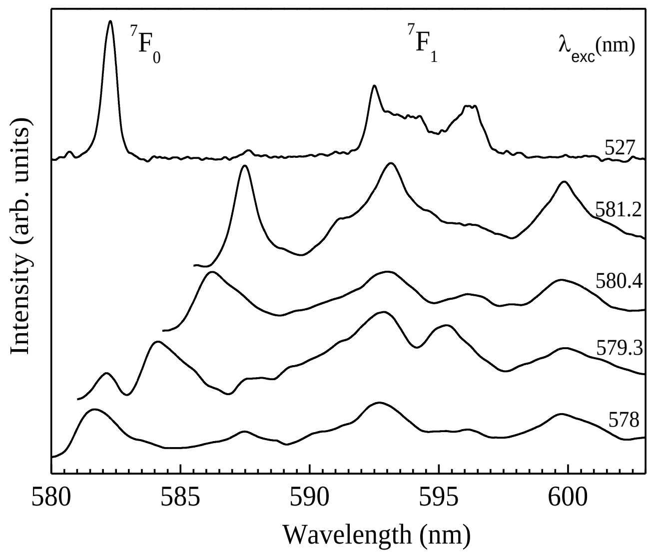

$^7F_0$
$^7F_1$
λ_{exc}(nm)
527
581.2
580.4
579.3
578
Intensity (arb. units)
580
585
590
595
600
Wavelength (nm)

Fig. 7

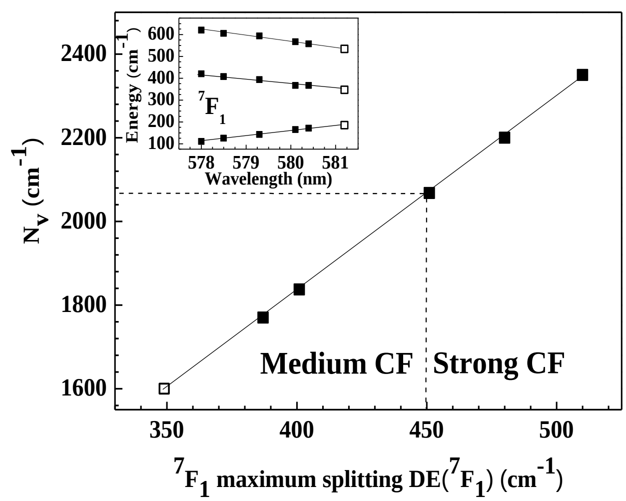

2400
2200
2000
1800
1600
N_V (cm^{-1})
350
400
450
500
$^7F_1$ maximum splitting DE($^7F_1$) (cm^{-1})
Medium CF
Strong CF
600
500
400
300
200
100
Energy (cm^{-1})
$^7F_1$
578
579
580
581
Wavelength (nm)

Fig. 8

Figure captions

Fig. 1. (color online) Cubic bixbyite structure of Y_2O_3. O correspond to small (red) atoms while Y correspond to large (blue) atoms. Dark blue atoms are those located at C_2 sites while light blue atoms are those located at S_6 sites.

Fig. 2. (a) TEM micrograph, (b) particle size histogram, (c) HRTEM micrographs, and (d) SAED pattern of the Y_2O_3 nanoparticles grown at 550 ºC.

Fig. 3. (color online) XRD patterns of Eu^{3+}-doped Y_2O_3 nanoparticles at different synthesis temperatures. Inset shows the variation of the lattice parameter for the different synthesis temperatures.

Fig. 4. Raman spectra of undoped Y_2O_3 and Eu^{3+}-doped Y_2O_3 nanophosphors obtained at different synthesis temperatures. Inset shows a zoom of the most intense Raman peak in undoped nano-crystals.

Fig. 5. (color online) $^5D_0 \rightarrow {}^7F_J$ (J=0-4) emission spectra of Y_2O_3 nano-phosphors doped with 1 at. wt% of Eu^{3+} ions annealed at 500 ºC (red) and 1000 ºC (black) for 2 h under broadband excitation of the $^5D_0 \rightarrow {}^5L_6$ transition at 395 nm at RT. Inset shows the $^5D_0 \rightarrow {}^7F_{0,1}$ emission spectra of the nano-phosphors annealed at 500, 600, 800 and 1000 ºC for 2 h corresponding to sizes of 6, 13, 21, and 37 nm, respectively.

Fig. 6. Inhomogeneous excitation profile of the $^7F_0 \rightarrow {}^5D_0$ transition in an Y_2O_3 nano-phosphor doped with 1 at. wt% of Eu^{3+} at 13 K.

Fig. 7. FLN emission spectra to the ^7F_J (J=1, 2) levels exciting selectively the $^5D_0$ level in an Y_2O_3 nano-phosphor doped with 1 at. wt% of Eu^{3+} at 13 K. Spectra are normalised to the maximum of the high-energy peak of the $^5D_0 \rightarrow {}^7F_1$ transition. Excitation wavelength is indicated for each spectrum in nm. The upper spectrum has been obtained exciting selectively the $^5D_1$ level at 527 nm in an Y_2O_3 nano-phosphor doped with 1 at. wt% of Eu^{3+} at 13 K.

Fig. 8. Scalar crystal-field strength parameter N_V as a function of the $^7F_1$ maximum splitting $\Delta E(^7F_1)$. The solid line indicates the fit to the theoretical expression of Malta *et al*. (see text). Inset shows the $^7F_1$ splitting as a function of the $^5D_0$ excitation wavelength. Open squares indicate those values associated to the Eu^{3+} ions at the 'true' C_2 site.

Table I. *Ab initio* theoretical (theo.) and experimental (exp.) frequencies of Raman modes in Y_2O_3. Experimental Raman modes frequencies for bulk Y_2O_3 of Ref. 19 have been added for comparison.

Peak /mode	ω(theo.) cm^{-1}	ω(exp.) cm^{-1}	ω(exp.)[a] cm^{-1}
F_g	125.7		116
F_g	133.4		129
A_g	156.0		161
F_g	178.5		179
E_g	191.2		193
F_g	230.5		
F_g	238.2		
F_g	313.8	318	318
F_g	320.0		
E_g	326.8	329	329
F_g	348.8		
A_g	356.3		
F_g	378.7	376	376
E_g	382.3		
F_g	392.6		399
A_g	419.6		
F_g	430.0	429	429
F_g	460.2	469	469
F_g	521.3		526
A_g	554.5	564	564
E_g	559.9	564	564
F_g	583.3	591	591